

On Maximizing Safety in Stochastic Aircraft Trajectory Planning with Uncertain Thunderstorm Development

Daniel Hentzen, Maryam Kamgarpour, Manuel Soler, Daniel González-Arribas^{a,b,c,d}

^aAutomatic Control Lab, ETH Zurich, Zurich, Switzerland. e-mail: dhentzen@ethz.ch

^bAutomatic Control Lab, ETH Zurich, Zurich, Switzerland. e-mail: mkamgar@control.ee.ethz.ch

^cDepartment of Bioengineering and Aerospace Engineering, Universidad Carlos III de Madrid, Leganés, Spain. e-mail: masolera@ing.uc3m.es

^dDepartment of Bioengineering and Aerospace Engineering, Universidad Carlos III de Madrid, Leganés, Spain. e-mail: daniel.gonzalez.arribas@uc3m.es

Abstract

Dealing with meteorological uncertainty poses a major challenge in air traffic management (ATM). Convective weather (commonly referred to as storms or thunderstorms) in particular represents a significant safety hazard that is responsible for one quarter of weather-related ATM delays in the US. With commercial air traffic on the rise and the risk of potentially critical capacity bottlenecks looming, it is vital that future trajectory planning tools are able to account for meteorological uncertainty. We propose an approach to model the uncertainty inherent to forecasts of convective weather regions using statistical analysis of state-of-the-art forecast data. The developed stochastic storm model is tailored for use in an optimal control algorithm that maximizes the probability of reaching a waypoint while avoiding hazardous storm regions. Both the aircraft and the thunderstorms are modeled stochastically. The performance of the approach is illustrated and validated through simulated case studies based on recent nowcast data and storm observations.

Keywords: Stochastic storm modeling, Stochastic optimal control, Aircraft trajectory planning

1. Introduction

A challenging aspect of tactical aircraft trajectory planning¹ is the avoidance of hazardous convective weather regions, more commonly referred to as storms or thunderstorms². The inherently uncertain nature of thunderstorms causes major safety risks. Strong conflicting up- and downdrafts lead to heavy turbulence. Hail, severe icing and lightning can also inflict significant damage to aircraft equipment and windshields. In addition to increased safety risks, thunderstorms are also a leading cause of reduced time (National Research Council (2003)) and cost (Michalek and Balakrishnan (2009)) efficiencies. From 2008 to 2013, inclement weather caused 69% of system-impacting delays (delays greater than 15 minutes), as recorded in the *OPSNET Standard "Delay by Cause" Reports*³. Within those weather delays, thunderstorms emerging from atmospheric instabilities were responsible for around 25%, turning them into the leading cause of flight delays in the US airspace.

Today, commonly used approaches to plan trajectories in the presence of thunderstorms are suboptimal and prone to human error. Thunderstorms are typically detected by satellite images or weather radar signals, which are processed into graphical images. The identified *thunderstorm cells* are then classified

according to severity. Regions of airspace that are considered to pose a significant safety hazard are recommended as unsafe-to-fly regions to air traffic controllers (ATCO) and pilots (Krozel and Mitchell (2007)).

In many cases these regions are avoided by manual trajectory modifications. This involves increased workload and potential loss of situational awareness for both ATCOs and pilots, jeopardizing safety and air traffic capacity.

One of the key concepts of future Air Traffic Management (ATM) systems is the so-called *trajectory-based operations* (TBO) described in the SESAR (European Commission and Eurocontrol (2015)) or NextGen (Joint Planning and Development Office (2012)) ATM master plans. The TBO concept will give aircraft the autonomy to update their trajectories to satisfy business needs, such as fuel or flight time savings, or to avoid potential conflicts or hazardous weather regions. Robust planning that accounts for the uncertainty associated to aircraft motion and thunderstorm development is paramount for a successful transition to TBO.

In McNally et al. (2015), the authors reported two years of operational testing of a tool coined *Dynamic Weather Routes* at American Airlines. The tool is a ground-based real-time trajectory automation system that continuously analyzes en-route aircraft. It computes simple corrections to flight plans to avoid thunderstorms while ensuring conflict avoidance, respecting airspace constraints and minimizing delay. However, the tool neither accounts for weather uncertainty, nor does it use advanced control and optimization algorithms, thus leaving room for improvement in the system's efficiency, safety, and

¹By *tactical* we refer to 10 minutes to 1 hour prior to the potential hazard encounter.

²Throughout this paper we will use the more general term *thunderstorm* to describe convective weather regions.

³NextGen Weather - Weather Delays <https://www.faa.gov/nextgen/programs/weather/faq/>

capacity.

The lack of probabilistic forecast data is one of the main bottlenecks in the development and full-scale deployment of automated trajectory planning tools that account for thunderstorm uncertainty. Today's state-of-the-art meteorological forecast products include current observations of the thunderstorm cells as well as predictions for their locations at discrete forecast horizons. A commonly used approach relies on deterministic short term forecasts, so-called nowcasts. They provide information on thunderstorm cell positions for up to a few hours ahead (Wilson et al. (1998)). Examples for such nowcast systems include the satellite data-based cloud tracker Cb-TRAM (Cumulonimbus Tracking and Monitoring) Zinner et al. (2008); and the radar-based Rad-TRAM (Radar Tracking and Monitoring), developed by Kober and Tafferner (2009). Nevertheless, these forecast products do not provide any uncertainty quantification.

The integration of stochastic information in meteorological forecast products has indeed proven difficult, mainly due to the short lifespan of convective phenomena (around 30 minutes) and an imperfect knowledge of the atmosphere at macroscopic scale. Recent efforts in this direction include, e.g., Mecikalski et al. (2015); Osinski and Bouttier (2018). The former presented two statistical learning approaches that incorporate numerical weather prediction (NWP) input within satellite images to produce probabilistic forecasts. Osinski and Bouttier (2018) presented an experimental product developed by Météo-France. It combines the numerical weather prediction model AROME-NWC with simulated radar images and post-processing. An ensemble of time-lagged forecasts with thunderstorm development information is then produced. Besides these efforts in combining data-driven methods and NWP, pure data-driven methods can be also used to model uncertainties in forecast products through comparison of actual instances of thunderstorms and their predictions.

The authors in Radhakrishna et al. (2012) investigated statistical properties of thunderstorm cells' growth and decay, as well as their scale dependence and predictability. They concluded that forecast accuracy of deterministic, radar-based nowcasts can be improved by the extrapolation of growth and decay for a few hours. In Sauer and Hauf (2014), the authors analyzed the error of radar-based nowcasts and their increasing uncertainty with time by determining spatial deviations of the nowcast predictions compared to the observed thunderstorm realizations. The authors argued that thunderstorm cells could be enlarged by an uncertainty margin that is dependent on the desired probability of avoiding the respective thunderstorm cell. In B. Zhang and Roemer (2014); Zhang et al. (2017), the authors introduced a probabilistic analysis of weather forecasting. The analysis is based on ensemble weather forecasting data provided by the Center for Analysis and Prediction of Storm (CAPS) Jung et al. (2008). Additionally, Zhang et al. (2017) presented a path planning algorithm to avoid the stochastic hazard, including a mission risk analysis. Nevertheless, additional efforts are needed in stochastic thunderstorm modeling and aircraft trajectory planning, e.g., considering the additional uncertainty introduced by the aircraft dynamic system.

Several methods to address aircraft path planning subject to uncertainties in system dynamics and obstacles (such as unsafe-to-fly regions) have been proposed. The problem of routing an aircraft to a target while avoiding uncertain hazardous weather zones in the presence of wind disturbance can be cast as the optimal control of a stochastic dynamic system through probabilistic obstacles, such as unsafe-to-fly regions. The following challenges arise: First, both the aircraft dynamics and the thunderstorm cells are nonlinear and non-convex. Second, the use of stochastic models is required, resulting in a theoretically and computationally challenging *stochastic optimal control* problem.

A possible approach is to bound the uncertain obstacles with deterministic sets. The authors in Kuwata et al. (2005) presented a receding horizon control strategy for aircraft trajectory planning in environments with unknown but bounded disturbances. The authors in Kamgarpour et al. (2010) proposed a receding horizon framework for designing safe aircraft trajectories. They took into account a dynamic weather forecast product to determine deterministic bounds for the thunderstorm regions to be avoided. While this set-bounded approach offers a high degree of safety, the solutions often degrade overall performance due to high conservatism arising from the protection against low probability uncertainty outliers. More importantly, the optimization problem can quickly become infeasible, for example in a scenario featuring a high number of obstacles. Such scenarios call for a solution that minimizes the risk of failure, instead of trying to eliminate it entirely. In Liu and Hwang (2014), a stochastic optimal control framework for mid-air conflict resolution was presented that could incorporate uncertainties in both aircraft and wind dynamics. However, in the studied aircraft-weather conflict, the weather hazard was considered deterministic. In Nilim et al. (2002), the authors addressed the problem of generating aircraft trajectories using a Markov decision problem where the evolution of the thunderstorms was modeled as a Markov chain. The transition probabilities were extracted from historical data using maximum-likelihood estimators. However, these probabilities were assumed stationary. Moreover, delay was used as the objective to be minimized. Given the uncertainties in thunderstorm development, an important objective is to minimize the probability of intersecting a hazardous weather region.

A suitable approach to generate trajectories that reach a target set while minimizing the probability of intersecting probabilistic unsafe-to-fly regions is to formulate a *stochastic reach-avoid problem*. The authors in Summers et al. (2011) considered a stochastic reach-avoid problem with a time-varying stochastic obstacle set. The problem was reformulated as a finite horizon stochastic optimal control problem and solved with Bellman's Dynamic Programming principle. We proposed this method as a feasible approach to aircraft trajectory planning in the presence of a single hypothetical thunderstorm, modeled by a stochastic ellipse Gonzalez-Arribas et al. (2017). However, in this preliminary study, we assumed a priori knowledge of the stochastic unsafe-to-fly regions. No forecast data was incorporated to define stochastic unsafe-to-fly regions. Furthermore, the approach did not address trajectory planning in the presence

of multiple thunderstorm regions.

The contribution of the paper is twofold: First, we propose a method for modeling thunderstorm in a stochastic manner. The method accounts for uncertainty in both the movement and, crucially, in the growth or decay of the thunderstorm cells. It is based on statistical analysis of historical nowcast data and its comparison with actual thunderstorm observations. Second, we combine the developed stochastic thunderstorm model with an optimal trajectory planning algorithm based on the stochastic reach-avoid methodology by Summers et al. (2011). The resulting aircraft trajectories maximize the probability of reaching a given waypoint while avoiding multiple thunderstorms, taking into account uncertainties in both the system dynamics (due to wind disturbance) and the unsafe-to-fly regions (due to uncertainties in nowcast data on thunderstorms). The resulting trajectories are validated against actual realizations of thunderstorms.

The paper is structured as follows: The proposed stochastic thunderstorm model derived from nowcast data is presented in Section 2. The stochastic reach-avoid framework, in which the aircraft trajectory generation is cast as a stochastic optimal control problem, is presented in Section 3. The trajectory planner, resulting from the integration of the stochastic thunderstorm model and the optimal control algorithm into one framework, is applied to two flight scenarios using historical forecast data in Section 4. Conclusions and future research directions are discussed in Section 5.

2. Stochastic Thunderstorm Modeling

The unsafe-to-fly regions to be avoided by the aircraft are hazardous convective weather regions, referred to as *thunderstorm cells*. The actual position and size of these regions, as well as an extrapolation of their position at different forecast horizons, are provided in the form of *nowcasts*. A nowcast file contains observations of the current state of the hazardous thunderstorm cells that are present in a particular portion of the airspace (here denoted by the 2D flight level $X \times Y$). These observations include, among others, the position of each thunderstorm cell center (in longitude, latitude coordinates), the extremities of each thunderstorm cell in all four directions (given in longitude, latitude), the size of each thunderstorm cell (expressed in number of “pixels”), a mean radius, as well as the speed and direction of each thunderstorm cell. Figure 1 depicts these thunderstorm cell characteristics. A nowcast file also provides a series of extrapolated predictions at discrete forecast horizons. However, these predictions are limited to the position of the thunderstorm cell centers. No other thunderstorm cell parameters are predicted. Every 10 minutes, a new nowcast file is published. Each nowcast file gives predictions for 6 forecast horizons from 10 to 60 minutes with a 10 minute spacing. Compared to the eventual observations of the thunderstorms, these forecasts feature significant prediction errors, mainly due to the nonlinear growth and decay of rainfall field size, which according to Browning et al. (1982) account for up to a quarter of the forecast error. This motivates the use of a stochastic model to represent the thunderstorm obstacles.

We consider a constant altitude flight, and thus, a two-dimensional domain. We aim to evaluate the probability that any discrete region of the flight level will be affected by hazardous thunderstorm at different forecast horizons $\tau = 1, 2, \dots, N$, corresponding to the forecast times 10, 20, \dots , 60 minutes and interpolated time instances in between. Figure 2 illustrates the nowcast structure and notation. Let $\Xi_{t_0+\tau|t_0}$ be the set of 2D obstacle regions capturing the thunderstorm forecast for time $t_0+\tau$ in the nowcast published at time t_0 . For the sake of brevity, we define $\square_\tau := \square_{t_0+\tau|t_0}$ throughout the paper. Let $X \times Y$ denote the 2D airspace under consideration. At each time instance t , we assign to each discretized coordinate $(x, y) \in X \times Y$ a thunderstorm probability, that is, the probability that the position (x, y) is in a thunderstorm cell. For this purpose we use the function $p_{\Xi_\tau}(x, y) : X \times Y \mapsto [0, 1]$. To compute $p_{\Xi_\tau}(x, y)$ for $\tau = 1, \dots, N$, starting from a known and deterministic initial obstacle set Ξ_0 , a stochastic model that describes the evolution of the thunderstorm is needed.

All information on thunderstorm position, size and movement is drawn from the available nowcasts. The analysis herein relies on a data sample of 720 nowcast files collected between December 15th and December 19th 2016, provided by the Spanish meteorological agency, *Agencia Estatal de Meteorología* (AEMET). AEMET’s YRADAR application produces both a 2D and a 3D analysis. Due to the simplifying assumption of constant altitude, the following analysis will be constrained to the 2D dataset. Due to the short average lifespan of thunderstorm cells, a significant proportion of detected cells disappear after the 40 minute horizon, rendering the data for the 50 and 60 minute horizons sparse. We will therefore restrict the analysis to a forecast horizon up to 40 minutes. The most relevant nowcast parameters used for the stochastic characterization of the storm cells are presented in Table 1.

We represent the thunderstorm cells using two states:

1. the position of the cell center (x_t^c, y_t^c) at time t ,
2. the position of the thunderstorm cell’s lateral and longitudinal extremities $(x_t^{(E)}, x_t^{(W)}, y_t^{(N)}, y_t^{(S)})$ at time t .

While no information on the thunderstorm cell’s shape is available, the four extremities enable us to formulate a rectangular bound of the thunderstorm cell. At time $t = t_0$ (t_0 being the time at which the nowcast is published), we have deterministic knowledge (assumed exact) of all six state variables. For times $t = t_0 + \tau$ ($\tau = 1, \dots, N$), the nowcast files provide a predic-

Table 1: Overview of relevant nowcast parameters.

Nowcast parameter	Description
NUM	ID of the cell
NUPIX	Number of pixels of the cell
LATCEN, LONCEN	Latitude/longitude of cell’s center
RADIOE	Effective radius of the cell
LATNOR, LATSUR	Limits of the cell in latitude
LONOES, LONEST	Limits of the cell in longitude
LAT10, LON10	Forecast for center after 10 min.
LAT20, LON20	Forecast for center after 20 min.
⋮	⋮
LAT60, LON60	Forecast for center after 60 min.
DIRN	Direction of displacement of the storm cell
V(KMH)	Velocity of displacement of the storm cell

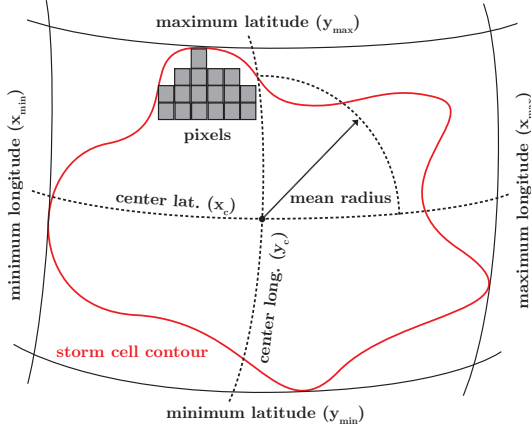


Figure 1: Thunderstorm cell representation

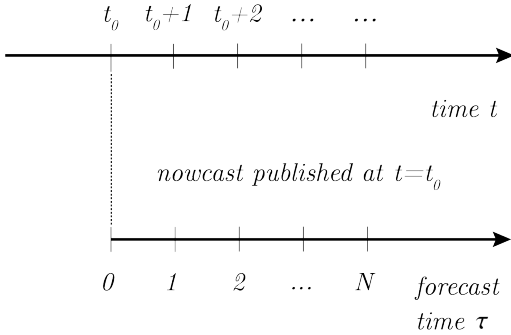


Figure 2: Nowcast structure.

tion of the thunderstorm cell centers but no information on the thunderstorm cell extremities. To account for the prediction error on the center position (increasingly significant with growing forecast horizon) and the lack of extremity predictions, we aim to formulate a stochastic dynamic model, which will allow us to predict the evolution of the thunderstorm cell state in a probabilistic fashion. By using this model in combination with a sampling-based method, we will be able to compute the probability of thunderstorm at each $(x_t, y_t) \in X \times Y$ for each time instance $t = t_0 + \tau$, that is, $p_{\Xi_t}(x, y)$.

2.1. Modeling Stochastic Thunderstorm Cell Dynamics

Let $\mathbf{c}_t = (x_t^c, y_t^c) \in \mathbb{R}^2$ denote the observed center of the thunderstorm cell at time t , where c denotes the center. Let \mathbf{c}_τ denote the forecast made at time t_0 for the thunderstorm cell center \mathbf{c} at time $t_0 + \tau$. Recall that $\tau = 1, 2, \dots, N$ is the forecast horizon corresponding to the forecast times 10, 20, \dots , 40 minutes and interpolations in between.

The forecast dynamics for the (observed) thunderstorm cell center position is given by $\mathbf{c}_{t_0+\tau} = \mathbf{c}_\tau + \eta_\tau$, where $\eta_\tau = (\eta_{\tau,x}, \eta_{\tau,y})$ denotes the prediction error associated with the forecast horizon τ in x and y directions. The prediction error grows with the length of the forecast horizon (Sauer and Hauf (2014); Radhakrishna et al. (2012)). It may also be dependent on current

meteorological conditions, such as strong wind in a particular direction. In the developed model, this error is accounted for by sampling it from a parameterized probability distribution and adding it to the nowcast prediction. The distribution type is determined by analyzing historical predictions and comparing them with the observations. Once an appropriate distribution type has been determined, the parameters of the distribution are determined and updated in real time using maximum likelihood estimation.

The forecast error at forecast horizon τ is given by $\eta_\tau = \mathbf{c}_{t_0+\tau} - \mathbf{c}_\tau$. Figure 3 shows combined scatter plots and histograms illustrating the deviation in longitude and latitude of the forecast center positions compared to the observed realizations in the training set for forecast horizons 10, 20, 30 and 40 minutes. Using Matlab's `allfitdist` function, all valid parametric probability distributions are fitted over the empirical data and compared for goodness-of-fit, as quantified by the Bayesian information criterion (BIC), a criterion for selecting a model among a finite set of models. The *logistic* distribution offers the best fit for the available data (see (Hentzen, 2017, Chapter 3) for a detailed discussion, where logistic, tlocation-scale, normal and generalized extreme value distribution fittings are presented, compared, and discussed). In particular, it is able to better account for the heavier tails compared to a normal distribution.

The probability density function (PDF) $f_{\mathcal{L}}$ of the *logistic* distribution \mathcal{L} is given by

$$f_{\mathcal{L}}(\eta; m, s) = \frac{1}{4s} \operatorname{sech}^2\left(\frac{\eta - m}{2s}\right) = \frac{e^{-\frac{\eta-m}{s}}}{s(1 + e^{-\frac{\eta-m}{s}})^2},$$

where $\eta \in \mathbb{R}$ is the forecast error, m is the mean of the distribution and $s \geq 0$ is the *scale* or *dispersion* parameter. The standard deviation σ is expressed by $\sigma = \frac{s\pi}{\sqrt{3}}$. The distribution's parameters are determined using maximum likelihood estimation with a defined number of historical data points. Based on the studied data samples, we conclude:

1. The thunderstorm cell center position prediction error in x and y directions $\eta_{\tau,x}$ and $\eta_{\tau,y}$ at forecast horizon τ can be approximated by sampling from the logistic PDFs \mathcal{L}_x^c and \mathcal{L}_y^c associated to the forecast horizon τ : $\eta_{\tau,x} \sim \mathcal{L}_x^c(\tau)$, $\eta_{\tau,y} \sim \mathcal{L}_y^c(\tau)$.
2. The parameters of these distributions (mean and scale) at different forecast horizons are computed using maximum likelihood estimation.

As the available nowcasts offer no forecast on thunderstorm cell size, past observations have to be analyzed to identify and extrapolate a growth or decay trend.

In the following analysis, growth and decay are expressed in terms of the change in lateral and longitudinal size of a single thunderstorm cell. Longitudinal size (width w) and lateral size (height h) at time t are defined using the nowcast extremity data:

$$w_t = x_t^{(E)} - x_t^{(W)}, \quad h_t = y_t^{(N)} - y_t^{(S)}.$$

The dynamics of the thunderstorm cell size are given by

$$w_{t+1} = w_t + \Delta w, \quad h_{t+1} = h_t + \Delta h,$$

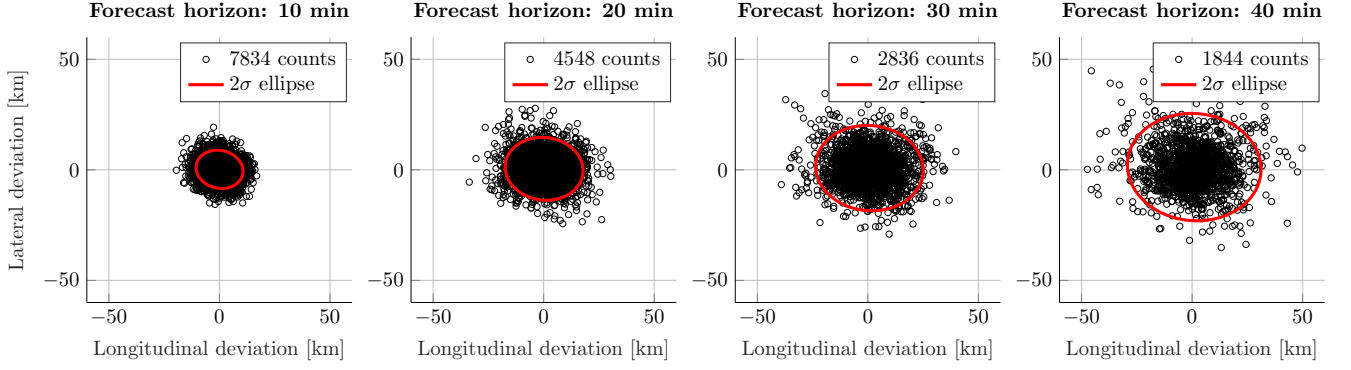


Figure 3: Longitudinal and lateral deviation of forecast thunderstorm cell center positions to observed realizations over growing forecast horizon.

where Δw and Δh denote the change in width and height, respectively. They are the stochastic parameters to be extrapolated from historical data.

Similar to the analysis of the thunderstorm cell center prediction error above, we determine an appropriate parameterized probability distribution to model Δw and Δh . The BIC indicates that the logistic probability distribution offers a superior fit to the normal distribution (see Hentzen (2017) for a detailed discussion). We observe that thunderstorm cells featuring a large surface area (expressed using the number of pixels on the radar images) grow or decay faster than smaller cells. We thus choose the parameters of the *logistic* distribution as a function of the thunderstorm cell size in pixels (s_{pix}):

$$\Delta w \sim \mathcal{L}^w(s_{pix}) \quad \Delta h \sim \mathcal{L}^h(s_{pix}).$$

The scale parameter of the Δh and Δw distributions is assumed to grow logarithmically with thunderstorm cell size (see Hentzen (2017)).

The derived stochastic model of the thunderstorm cell dynamics is given by two steps as follows.

1. Sample step:

$$\begin{aligned} \eta_{\tau,x} &\sim \mathcal{L}_x^c(\tau), & \eta_{\tau,y} &\sim \mathcal{L}_y^c(\tau) \\ \Delta w &\sim \mathcal{L}^w(s_{pix}), & \Delta h &\sim \mathcal{L}^h(s_{pix}) \end{aligned}$$

2. Update step:

$$\begin{aligned} \begin{cases} \begin{bmatrix} x_{t_0+\tau}^c \\ y_{t_0+\tau}^c \end{bmatrix} \\ \text{corrected centers} \\ \text{at forecast horizon } \tau \end{cases} &= \begin{cases} \begin{bmatrix} x_{t_0+\tau}^c \\ y_{t_0+\tau}^c \end{bmatrix} \\ \text{uncorrected centers} \\ \text{at forecast horizon } \tau \end{cases} + \begin{cases} \begin{bmatrix} \eta_{\tau,x} \\ \eta_{\tau,y} \end{bmatrix} \\ \text{sampled error} \end{cases} \\ \\ \begin{cases} \begin{bmatrix} x_{t_0+\tau}^{(W)} \\ x_{t_0+\tau}^{(E)} \\ y_{t_0+\tau}^{(S)} \\ y_{t_0+\tau}^{(N)} \end{bmatrix} \\ \text{corrected extremities} \\ \text{at forecast horizon } \tau \end{cases} &= \begin{cases} \begin{bmatrix} x_{t_0+\tau}^c \\ x_{t_0+\tau}^c \\ y_{t_0+\tau}^c \\ y_{t_0+\tau}^c \end{bmatrix} \\ \text{width/height} \\ \text{at } t_0 \end{cases} + \begin{cases} \begin{bmatrix} -x_{t_0}^c + x_{t_0}^{(W)} \\ x_{t_0}^c - x_{t_0}^{(E)} \\ -y_{t_0}^c + y_{t_0}^{(S)} \\ y_{t_0}^c - y_{t_0}^{(N)} \end{bmatrix} \\ \text{sampled change} \\ \text{in width/height} \\ \text{over forecast horizon } \tau \end{cases} + \frac{1}{2} \begin{cases} \begin{bmatrix} -\sum_{i=1}^{\tau} \Delta w(s_{pix}) \\ \sum_{i=1}^{\tau} \Delta w(s_{pix}) \\ -\sum_{i=1}^{\tau} \Delta h(s_{pix}) \\ \sum_{i=1}^{\tau} \Delta h(s_{pix}) \end{bmatrix} \end{cases} \end{aligned}$$

2.2. Obstacle Clustering

The dynamic thunderstorm cell model provides a sequence of predictions of thunderstorm cell positions and sizes for $t = t_0 + \tau$ with $\tau = 1, \dots, N$. However, the individual thunderstorm cells alone are not suitable obstacles for scenarios with a high density of convective weather. The thunderstorm cells are often grouped closely together in the airspace affected by convective weather. If every thunderstorm cell were to be considered as an individual obstacle, the resulting safety-optimal trajectory would likely contain a high number of turn advisories, as individual obstacles would have to be avoided every few minutes. Although such a trajectory might be feasible in theory, it is not an option in a realistic ATM setting. Furthermore, individual thunderstorm cells are likely to split into sub-cells or merge with other neighboring or overlapping cells. It is also likely that new thunderstorm cells appear in regions with high levels of convective weather. Nowcasts do not contain information on these processes. Considering the thunderstorm cells as individual obstacles would thus result in potentially unsafe trajectories. For these reasons, we propose a more robust approach in which the individual thunderstorm cells predicted for forecast horizons $\tau = 1, \dots, N$ by the dynamic thunderstorm cell model at time t_0 , are clustered into larger obstacles unsafe-to-fly regions. This clustering is updated at each forecast horizon τ to account for the movement of the individual thunderstorm cells. The clustering results in a sequence of obstacles unsafe-to-fly regions that represent areas of the airspace that feature a high density of thunderstorm cells and a high probability of thunderstorm occurrence. We use K-means clustering for this purpose.

At time $t_0 + \tau$, we forecast the individual thunderstorms ($\mathbf{o}_\tau^1, \mathbf{o}_\tau^2, \dots, \mathbf{o}_\tau^n$), where each element is a d -dimensional real vector. The n forecast thunderstorms are partitioned into $K \leq n$ clusters $\{C_\tau^1, C_\tau^2, \dots, C_\tau^K\}$ with centroids (that is, mean of points within the cluster) $\{\bar{\mathbf{o}}_\tau^1, \bar{\mathbf{o}}_\tau^2, \dots, \bar{\mathbf{o}}_\tau^K\}$ such that the variance of the distance of the observations within a cluster to the cluster's centroid is minimized:

$$\arg \min_C \sum_{k=1}^K \sum_{\mathbf{o}_\tau^i \in C_\tau^k} \|\mathbf{o}_\tau^i - \bar{\mathbf{o}}_\tau^k\|_2^2.$$

Above, $\|\cdot\|_2$ is the Euclidean 2-norm. For our application, we consider $\mathbf{o}_\tau = (x_\tau^c, y_\tau^c, \xi_\tau)$, where x^c and y^c are the x and y coordinates of the thunderstorm center and ξ is the heading of the thunderstorm, as provided in the nowcast. This choice allows to group the thunderstorms based on their distance to each other and based on the directions in which they are heading.

Choosing the number of clusters K is a hard algorithmic problem. A possible metric for the quality of the resulting clusters is the sum of squared errors (SSE), that is, the sum of the squared distance between each member of the cluster and its centroid. The SSE decreases with growing K , with $\text{SSE} = 0$ for $K = n$. Applying the so-called *elbow method*, we choose K at the *elbow point*, that is, where the SSE starts decreasing at a significantly slower rate. The elbow method is heuristic and is not guaranteed to give satisfactory results in all cases. We discuss an alternative, empirical method to determine K based on a parameter study with historical data in Hentzen (2017).

Let $\Xi_\tau = \{C_\tau^k\}$ for $k = 1, \dots, K$ and $\tau = 1, \dots, N$ be the new obstacle set containing the K elliptical obstacles unsafe-to-fly regions forecast for time $t_0 + \tau$ by the nowcast published at time t_0 . We now require a stochastic representation of the obstacle set, expressed by $p_{\Xi_\tau}(x, y)$. Recall that this function returns the probability that the coordinate (x, y) is within any obstacle cluster C_τ^k ($k \in 1, 2, \dots, K$) in Ξ_τ at time $t_0 + \tau$.

2.3. Stochastic Representation of Unsafe-to-fly Region Clusters

The computation of $p_{\Xi_\tau}(x, y)$ requires a prediction of the obstacle clusters' position at forecast horizons τ . This prediction in turn calls for a geometric description of the clusters. For this purpose, we choose minimum-volume ellipses (MVE) that enclose the extremities of the thunderstorm cells present within one cluster C_τ^k . Ellipses are preferred over polygons for the geometric obstacle characterization due to their efficient mathematical description. Figure 4 shows an example of MVE enclosing for two clusters.

Each ellipse \mathcal{E}_τ^k is parameterized by its center $\mathbf{m}_\tau^k \in \mathbb{R}^2$ and its positive definite eccentricity matrix M_τ^k . The position given by coordinate $\mathbf{x} = (x, y)$ is within an elliptic obstacle unsafe-to-fly region at time $t_0 + \tau$ if the following condition is fulfilled for any k :

$$\mathbf{x} \in \mathcal{E}_\tau^k(\mathbf{m}_\tau^k, M_\tau^k) \iff (\mathbf{x} - \mathbf{m}_\tau^k)^T M_\tau^k (\mathbf{x} - \mathbf{m}_\tau^k) \leq 1.$$

The objective is to compute p_{Ξ_τ} for the defined obstacle set at forecast horizons $\tau = 1, \dots, N$, that is, the probability

$$p_{\Xi_\tau} = P\{\mathbf{x} \in \mathcal{E}_\tau^k(\mathbf{m}_\tau^k, M_\tau^k)\} \quad \text{for some } k \in \{1, \dots, K\}.$$

To achieve this objective we introduce a sampling-based approach, here referred to as the *Minimum-Volume-Ellipse (MVE) sampling*. Every time a new nowcast file is published (at time instance t_0), clustering is applied for $t = t_0$ (the current observations of the thunderstorms) and for $t = t_0 + \tau$ with $\tau = 1, \dots, N$ (the thunderstorm's forecast at forecast horizons τ). Then, for each of the K clusters present at time $t + \tau$, we predict the position and size of all thunderstorms assigned to that cluster at forecast horizon τ using the stochastic thunderstorm cell model

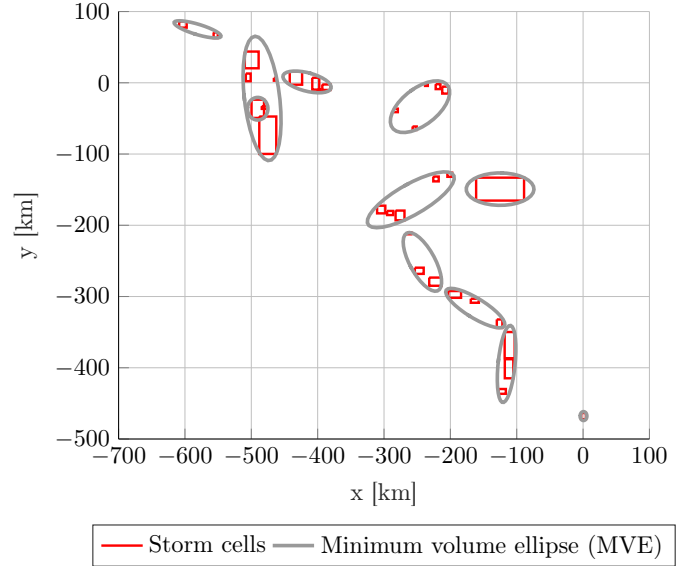


Figure 4: Minimum volume ellipse enclosing of clusters in nowcast data of December 19th 2016, 10:30 UTC

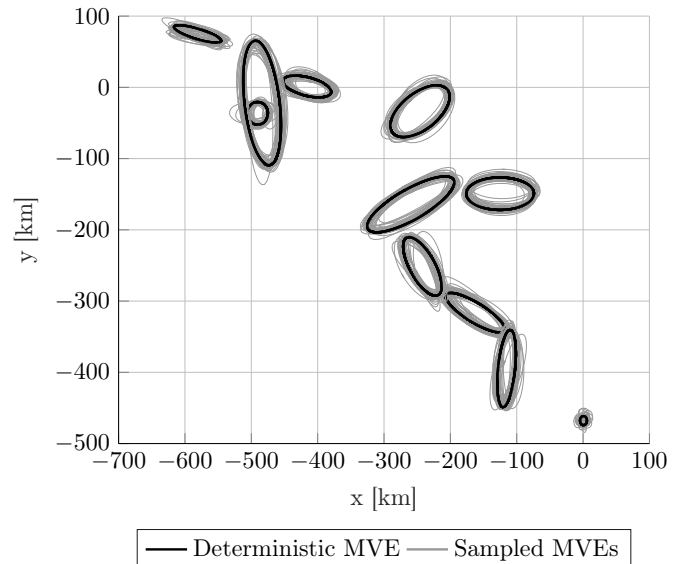


Figure 5: 50 MVE samples for forecast horizon 10 min.

in subsection 2.1. We then enclose the predicted thunderstorms with K MVEs. This procedure is repeated n_s times at each forecast horizon τ , resulting in n_s different MVEs per obstacle cluster. We can then apply Monte Carlo methods to compute the probability $p_{C_\tau^k}(x, y)$ of coordinate $(x, y) \in X \times Y$ being within the obstacle cluster C_τ^k at time $t_0 + \tau$.

Figure 5 shows an example for such MVE realizations for a forecast horizon index τ equivalent to 10 minutes. The black ellipses bound the clustered thunderstorms as provided by the deterministic (uncorrected) data in the nowcast. For each cluster, $n_s = 50$ realizations of the thunderstorm development up to the forecast horizon of 10 minutes are sampled and bounded by an MVE (depicted in grey). This allows to account for the uncertain evolution of the thunderstorms over the 10 minute hori-

zon.

Once the *MVE Sampling* algorithm has been applied to all K obstacle clusters within a nowcast for all forecast horizons $\tau = 1, 2, \dots, N$, the K individual functions $p_{C_\tau^k}$ for $k = 1, \dots, K$ at forecast horizon τ need to be merged into the function p_{Ξ_τ} that returns the probability of (x, y) being in any of the K clusters. We can now approximate the probability of a coordinate (x, y) being in any of the obstacle clusters as

$$p_{\Xi_\tau}(x, y) \approx 1 - \underbrace{\prod_{k=1}^K (1 - p_{C_\tau^k}(x, y))}_{\substack{\text{probability of no thunderstorm at } (x, y) \\ \text{probability of at least one thunderstorm at } (x, y)}}. \quad (1)$$

In the approximation above, we assume that the event of a coordinate (x, y) falling into a certain cluster is independent of the event of the same coordinate falling into another cluster. While the event that a storm cell is present in a certain region and travels in a certain direction is certainly not independent from the presence of other storm cells in the same region and their movements, we minimize this dependence within the clusters using K-means. Indeed, K-means maximizes the between-cluster variance of all the storm observation vectors, that is, $\mathbf{o} = (x^c, y^c, \xi_\tau)$. Furthermore, the above inequality is safely conservative. In particular, denoting stochastic events of (x, y) falling into clusters C_τ^k and C_τ^l , for $k, l \in \{1, \dots, K\}$, with A and B respectively, we have $P(A \cap B) = P(A|B)P(B)$. Since in this setting it is more plausible that $P(A|B) \geq P(A)$ (knowing a cell belongs to one storm cluster increases its probability of belonging to the other storm cluster at the same time), we conclude that $P(A \cap B) \geq P(A)P(B)$. Hence, $1 - P(A \cap B) \leq 1 - P(A)P(B)$ and $p_{\Xi_\tau} \geq p_{\Xi_{\tau, \text{real}}}$, where $p_{\Xi_{\tau, \text{real}}}$ is the true (unknown) probability. Therefore, our approximation yields an upper bound on the true probability of coordinate (x, y) being in any of the obstacle clusters. This will lead to a more conservative solutions but will not degrade safety.

Figure 6 shows an example of the probability function $p_{\Xi_\tau}(x, y)$ that results for the nowcast provided at 00:00 UTC on December 19th 2016, at a forecast horizon of 30 minutes. The pink, dark boxes indicate thunderstorm cells that were predicted in the original nowcast and indeed observed 30 minutes after the nowcast was issued. The green, light boxes indicate thunderstorm cells that were observed 30 minutes after the nowcast was issued, but not predicted in the nowcast. The figure illustrates the predictive performance of the developed algorithm and the robustness of the clustering approach to newly appearing thunderstorms that are not predicted in the nowcast.

3. Stochastic Reach-Avoid for Aircraft Trajectory Planning

3.1. Stochastic Dynamic Model

For the purpose of trajectory planning, we use a simplified model of aircraft dynamics, namely a simple point-mass unicycle model. Furthermore, we assume that the aircraft is flying at constant altitude and constant airspeed v . Let $S = X \times Y \times [-\pi, \pi] \subset \mathbb{R}^3$ be the state space of the system with

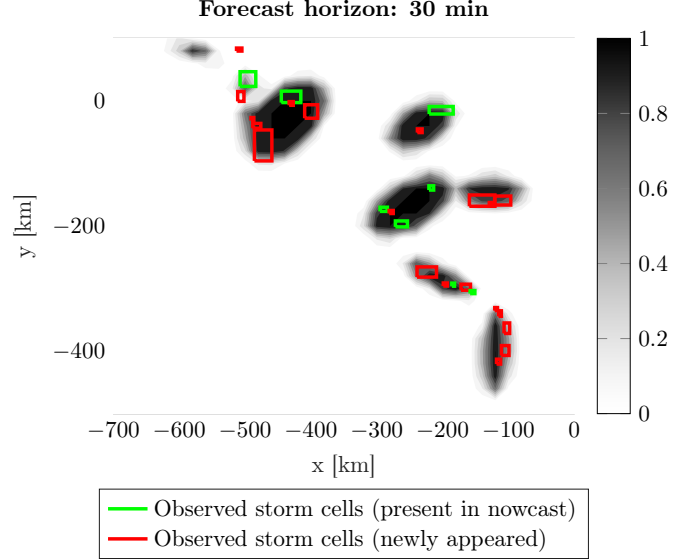


Figure 6: Probability of storm $p_{\Xi_{30}}$ for nowcast published on Dec. 19th 2016 at 00:00 UTC.

state $\mathbf{s} = [x, y, \lambda] \in S$, where $(x, y) \in X \times Y \subset \mathbb{R}^2$ is the two-dimensional position of the aircraft and $\lambda \in [-\pi, \pi]$ is its heading angle measured counter-clockwise from the geographic East. Consistent with current air traffic procedures, we consider three possible advisories: left turn, right turn and straight flight. Hence, we can represent the control space as $U = \{-\Omega, 0, \Omega\}$, with control input $u \in U$ representing the yaw rate. The dynamics of the aircraft in discrete time are given by

$$\begin{aligned} x_{t+1} &= x_t + \delta \cdot (v \cos(\lambda_t) + w_{u,t}) + \omega_t^1, \\ y_{t+1} &= y_t + \delta \cdot (v \sin(\lambda_t) + w_{v,t}) + \omega_t^2, \\ \lambda_{t+1} &= \lambda_t + \delta \cdot u_t + \omega_t^3, \end{aligned} \quad (2)$$

where δ is the sampling time used to discretize the continuous-time model, $w_{u,t}$ and $w_{v,t}$ denote zonal (West-to-East) and meridional (South-to-North) wind values, respectively, and $\omega_t = [\omega_t^1, \omega_t^2, \omega_t^3]$ is the disturbance of the system due to wind and model uncertainties. The noise component ω^3 accounts for possible actuation inaccuracies and the fact that the heading cannot be adjusted by the pilots in arbitrary small increments.

Given the stochasticity introduced by the disturbance term, the aircraft state at time $t+1$ can be equivalently captured using a so-called stochastic kernel χ . Let $\mathcal{B}(S)$ denote the set of all measurable subsets of the state space S . The stochastic kernel χ returns the probability of state \mathbf{s}_{t+1} being in subset $B \in \mathcal{B}(S)$, given the current state \mathbf{s}_t and the control input u_t . The discrete-time aircraft dynamics can thus equivalently be described by

$$\mathbf{s}_{t+1} \sim \chi(B|\mathbf{s}_t, u_t), \quad t = 0, 1, \dots, N.$$

We can state in familiar terms that the state \mathbf{s}_{t+1} is sampled from the probability distribution $\chi(\cdot|\mathbf{s}_t, u_t)$. The numerical computation of χ will be explained later in this section.

The unsafe-to-fly regions to be avoided by the aircraft are hazardous thunderstorm regions. A stochastic thunderstorm

model was derived in Section 2, which provided $p_{\Xi_\tau}(x, y) = P\{(x, y) \in \Xi_\tau\}$, the probability of coordinate $(x, y) \in X \times Y$ belonging to a thunderstorm cell at a given time $t_0 + \tau$. The probability of the state $\mathbf{s} = [x, y, \lambda]$ intersecting a thunderstorm can thus be computed as $p_{\Xi_\tau}(\mathbf{s}) = p_{\Xi_\tau}(x, y)$ for each $\lambda \in [-\pi, \pi]$.

3.2. The Reach-Avoid Problem and Solution

Let the sequence $\mu = \{\mu_0, \mu_1, \dots, \mu_{N-1}\}$ be a control policy, that is, a map $\mu_t : S \rightarrow U$ that returns a control input $u_t \in U$ for every state $\mathbf{s}_t \in S$ for $t = 0, \dots, N-1$. Given the stochastic kernel χ and the thunderstorm probability function p_{Ξ_τ} the reach-avoid objective is as follows. Find an optimal control policy that maximizes the probability of the aircraft reaching a goal set $G \subset S$ in N steps, while staying in a safe set Z_t for all time steps $t = 0, 1, \dots, N$. While the initial obstacle set Ξ_0 is assumed to be known and deterministic, the future obstacles are predicted using the parameterized stochastic thunderstorm cell model introduced in Section 2.

The reach-avoid probability for a given control policy μ and initial state \mathbf{s}_0, Ξ_0 is written mathematically as⁴

$$r_{\mathbf{s}_0, \Xi_0}(\mu) := P_{\mathbf{s}_0, \Xi_0}^\mu \{ \exists j \in [0, N] : \mathbf{s}_j \in G \\ \wedge \forall i \in [0, j-1] : \mathbf{s}_i \in Z_i \setminus G \}.$$

Let $\mathbf{1}_A$ denote the indicator function of the set A . It can be verified that

$$r_{\mathbf{s}_0, \Xi_0}(\mu) = \sum_{j=0}^N \left(\prod_{i=0}^{j-1} \mathbf{1}_{Z_i \setminus G}(\mathbf{s}_i) \right) \mathbf{1}_G(\mathbf{s}_j) \\ = \begin{cases} 1 & \text{if } \exists j \in [0, N] : \mathbf{s}_j \in G \wedge \forall i \in [0, j-1] \mathbf{s}_i \in Z_i \setminus G \\ 0 & \text{otherwise.} \end{cases}$$

Denoting by $p_{Z_i \setminus G}(\mathbf{s}_i) = \mathbf{1}_{Z_i \setminus G}(\mathbf{s}_i) - p_{\Xi_i}(\mathbf{s}_i)$ the probability of being in the safe set but not in the goal set, the above can equivalently be written as (see Summers et al. (2011) for a proof)

$$r_{\mathbf{s}_0, \Xi_0}(\mu) = E_{\mathbf{s}_0}^\mu \left[\sum_{j=0}^N \left(\prod_{i=0}^{j-1} p_{Z_i \setminus G}(\mathbf{s}_i) \right) \mathbf{1}_G(\mathbf{s}_j) \right].$$

To maximize the probability of safely reaching the target, we thus need to compute $r^*(\mathbf{s}_0, \Xi_0) := \max_\mu r_{\mathbf{s}_0, \Xi_0}(\mu)$. We achieve this by solving the stochastic optimal control problem via dynamic programming.

We define the optimal cost-to-go function $V_t^* : S \rightarrow [0, 1]$, $t = 0, \dots, N$. It maximizes $V_0^*(\mathbf{s}_0) := r_{\mathbf{s}_0, \Xi_0}(\mu)$. The backwards recursion needed to compute the optimal cost-to-go V_t^* for $t = N-1, \dots, 0$ is based on the dynamic programming principle of optimality. In particular,

$$V_N^*(\mathbf{s}) = \mathbf{1}_G(\mathbf{s}) \quad (3)$$

$$V_t^*(\mathbf{s}) = \mathbf{1}_G(\mathbf{s}) + p_{Z_t \setminus G}(\mathbf{s}) \max_{u \in U} \int_S V_{t+1}^*(\mathbf{s}') \cdot \chi(\mathbf{s}'|\mathbf{s}, u).$$

The corresponding optimal reach-avoid policy μ_t^* for $t = 0, \dots, N-1$ is given by

$$\mu_t^*(\mathbf{s}) \in \arg \max_{u \in U} \left\{ \mathbf{1}_G(\mathbf{s}) + p_{Z_t \setminus G}(\mathbf{s}) \int_S V_{t+1}^*(\mathbf{s}') \cdot \chi(\mathbf{s}'|\mathbf{s}, u) \right\}.$$

3.3. Numerical Implementation

To compute the above reachability probability, first we discretize the state space and compute the transition probability matrix $p_r(\mathbf{s}'|\mathbf{s}, u) : S \rightarrow [0, 1]$, where $\mathbf{s}, \mathbf{s}' \in S, u \in U$ denote state and input values at discretized points in the respective domains. The function $p_r(\mathbf{s}'|\mathbf{s}, u)$ is derived based on the transition kernel χ and maps to each (discretized) state \mathbf{s}' the probability of being reached at the next time step, given the current discretized state \mathbf{s} and control input values u . Next, we compute recursion (3) at discretized grid points using matrix multiplication and array maximization.

The state space S is discretized in all three dimensions X, Y , and $[-\pi, \pi]$ using the discretization sizes dx, dy and $d\lambda$, respectively. The process disturbance ω is drawn from a normal distribution \mathcal{N} with zero mean and covariance matrix Σ_ω (Summers et al. (2011)):

$$\omega = [\omega^1, \omega^2, \omega^3]^T \sim \mathcal{N}(0, \Sigma_\omega),$$

where $\Sigma_\omega = \text{diag}(\sigma_1^2, \sigma_2^2, \sigma_3^2)$, (σ denoting a standard deviation). Given the zero mean uncertainty, the mean state \mathbf{s}'_m that the aircraft will reach at the next time step given its current state $\mathbf{s} = [x, y, \lambda]$ and the control input u is

$$\mathbf{s}'_m = \begin{bmatrix} x + \delta \cdot v \cos(\lambda) + \delta \cdot w_u \\ y + \delta \cdot v \sin(\lambda) + \delta \cdot w_v \\ \lambda + \delta \cdot u \end{bmatrix}.$$

Using the probability density function of the multivariate normal distribution f_n with mean \mathbf{s}'_m and covariance Σ_ω , we obtain the discretized transition probability p_r in two steps:

$$p_{r,temp}(\mathbf{s}'|\mathbf{s}, u) = dx \cdot dy \cdot d\lambda \cdot f_n(\mathbf{s}'_m),$$

$$p_r(\mathbf{s}'|\mathbf{s}, u) = \frac{p_{r,temp}(\mathbf{s}'|\mathbf{s}, u)}{\sum_S p_{r,temp}(\mathbf{s}'|\mathbf{s}, u)}.$$

This is then used to compute the integral term in (3) as a summation over the state

$$\int_S V_{t+1}^*(\mathbf{s}') \cdot \chi(\mathbf{s}'|\mathbf{s}, u) \approx \sum_S V_{t+1}^*(\mathbf{s}') \cdot p_r(\mathbf{s}'|\mathbf{s}, u).$$

The other terms in computation of (3) are simply evaluations of a point belonging to a set or maximization over an array of numbers. Note that finer discretization grids result in larger matrix and array dimensions and hence more computational effort.

⁴The notation implies requirement on i is fulfilled when $\mathbf{s}_0 \in G$.

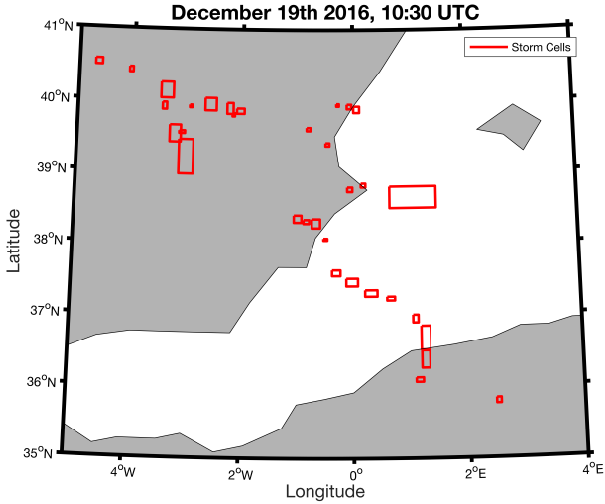


Figure 7: Illustration of storm cells in nowcast on Dec. 19th 2016, 00:00 UTC.

4. Case Studies

The developed trajectory planning tool is applied to two realistic flight scenarios using state-of-the-art nowcast data. The safety of the trajectories optimized based on stochastic control framework are compared against the actual storm observations.

The proposed algorithm is implemented in Matlab and simulated on an Intel Core i7 2.5 GHz processor with 16 GB RAM. All CPU times refer to this infrastructure.

4.1. Problem Setup

A region of airspace over the Spanish eastern coast and the Balearic sea, spanned by the corner coordinates $(-5^\circ, 41^\circ)$ and $(4^\circ, 35^\circ)$ is considered. This region is projected onto a 2D plane with a Lambert conformal projection centered at $(38^\circ, -98^\circ)$. The area of interest in $X \times Y$ coordinate is $[-650, 100] \times [-550, 200]$ (in km). To simulate a realistic scenario, the storm cell configuration is extracted from the AEMET nowcast of December 19th 2016 at 10:30 UTC, illustrated in Figure 7.

Flight 1: The initial condition of the aircraft is $\mathbf{s}_0 = (-365, 100, -1.92)$ rad heading directly to its goal set $G = [-490, -470] \times [-230, -210] \times [-\pi, \pi]$. From this starting position, the goal set is at 340 km of the starting point (26 min straight line flight at the chosen airspeed, without considering wind).

Flight 2: The aircraft starts at $\mathbf{s}_0 = (-100, 30, -2.5)$ rad heading directly to the same goal set as in Flight 1. In contrast to Flight 1, the aircraft starts further away from the goal set, at a distance of 455 km (35 min straight line flight at the given airspeed, without considering wind).

We model the aircraft using the discrete time unicycle dynamics presented in the previous Section, with an airspeed of 792 km/h and a maximal turn rate of 0.3 rad/min. As we are dealing with turn advisories, a low turn rate is chosen to enable a smooth passenger friendly trajectory. The disturbance parameters in aircraft dynamics in (2) are set to $\Sigma_\omega = \text{diag}(\sigma_1^2, \sigma_2^2, \sigma_3^2)$, with $\sigma_1^2 = \sigma_2^2 = 0.25 [m^2]$, $\sigma_3 = 4 \cdot 10^{-5} [rad^2]$. Wind forecast values are $w_{u,t} = 2.6$ m/s and $w_{v,t} = 5.6$ m/s for the zonal

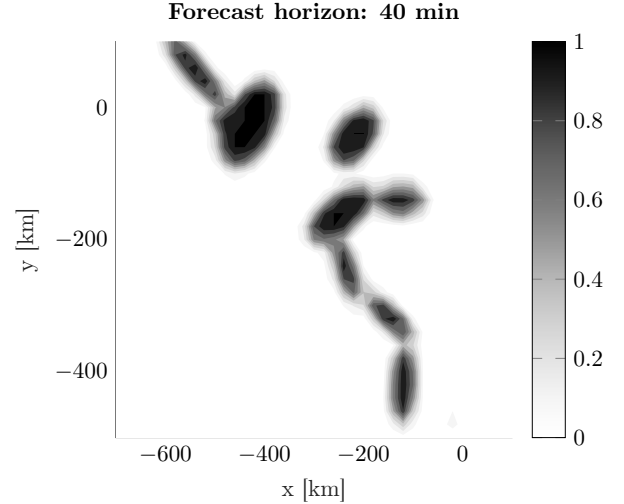


Figure 8: Probability of storm $p_{\Xi_{40}}$ computed with the coarse grid setting at forecast horizon of 40 minutes.

(West-to-East direction) and meridional (South-to-North direction) component, respectively. They are assumed to be constant over time and have been retrieved from the corresponding ECMWF Forecast as the average values in the area and time period of interest. At the specified true airspeed v and discretization time step of $\delta = 2$ min, the random variable corresponding to the distance covered by the aircraft in one time step has a 95% confidence interval 26.4 ± 1.74 km. At a yaw rate of $\Omega = 2.7$ rad/min, the random variable corresponding to the turning angle covered in one time step has a 95% confidence interval 5.4 ± 0.014 rad.

The time horizon is set to 40 minutes, equivalent to the maximum usable forecast horizon provided in the nowcast files. We note that the chosen time horizon may in theory be extended to an arbitrarily large value to fit any flight duration. However, we are constrained by the maximum forecast horizon provided in the available nowcast files. To illustrate the influence of the time horizon, flight 2 is simulated with both a forecast horizon of 40 minutes and the maximum allowable 60 minutes. Two simulation settings are used: Setting 1 uses a coarse discretization grid and a low number of samples and clusters, while setting 2 uses a very fine grid and a higher number of samples and clusters. Table 2 provides an overview of both settings.

4.2. Results

Figure 8 shows the *probability of storm* p_{Ξ_t} , in the considered airspace at a 40 minutes forecast horizon, computed with setting 2. The clusters and associated MVEs are clearly distinguishable. While the computation of the storm probability takes 279 s using the coarse setting 1, the simulation with the

Table 2: Overview of the two simulation settings.

Setting 1 - Coarse	Setting 2 - Fine
$33 \times 28 \times 32$ grid	$66 \times 56 \times 32$ grid
100 MVE samples	500 MVE samples
12 clusters	18 clusters

fine setting 2 significantly degrades computational performance (7'016 s) as seen in Table 3.

Figure 9 shows the *optimal reach-avoid probability* for flight 2. For every point of the map, this is the maximum probability of reaching the goal set safely. Next to the low probability areas that are due to likely storm presence, we observe the reachability limit in the form of a distinct boundary in the upper right corner. Indeed, given the fixed time horizon and the constant airspeed of the aircraft, the aircraft can only reach targets within a given distance starting with certain heading angle. We recompute the optimal reach-avoid probability for an extended time horizon of 60 minutes. Figure 9 shows that the mentioned reachability limit in the upper right corner has retreated. The aircraft can now safely reach the given goal set from a greater distance.

Runtime for the computation of the optimal reach-avoid probability increases with grid size, as shown in Table 3.

Flight 1; Setting 1. Figure 10 shows the mean trajectory and 2σ confidence bounds resulting from 10'000 trajectory simulations for flight 1 with setting 1. The red circles represent the observed storm cells at the given time. The grey ellipses are MVE samples (introduced in Section 2.3), that is, samples of possible future positions of the storm cell clusters. As discussed in Section 2.2, the developed algorithm generates trajectories that avoid these areas of high storm probability. This is illustrated in Figure 10: Accounting for the inherent uncertainty in the forecasts, the trajectory avoids not only individual predicted storm cells, but entire areas predicted to have high probability of storm. Almost all observed storm cells (depicted in red) fall into one of these areas. In this particular scenario, the trajectory is headed straight towards the goal set at first, following its reference trajectory. To avoid the approaching storm clusters, the aircraft then changes heading and passes through the opening between two clusters. Once the aircraft has passed the clusters, it changes heading once more to head to the goal set. This trajectory, if executed, would avoid all observed storm cells.

The optimal reach-avoid probability for the chosen initial condition is 1.00. All of the simulated trajectories reach the goal set within the specified horizon without hitting one of the observed thunderstorms. Table 4 provides an overview of the relevant simulation results.

Flight 1; Setting 2. The same flight is simulated with the fine settings.

Due to the improved resolution (higher number of clusters and smaller discretization size), more regions of the airspace are predicted to be safe. The resulting trajectory is therefore less conservative, passing closer to the storms and reaching the goal set 168 s earlier. The above comparison of a coarse and a

Table 3: Overview of computational performance.

	Setting 1	Setting 2
Probability of storm $p_{\Xi, \tau}$ ($\tau = 1, \dots, N$)	279 s	7'016 s
Reach-avoid probability $V_0^*(\mathbf{x}_0)$	1'196 s	9'101 s

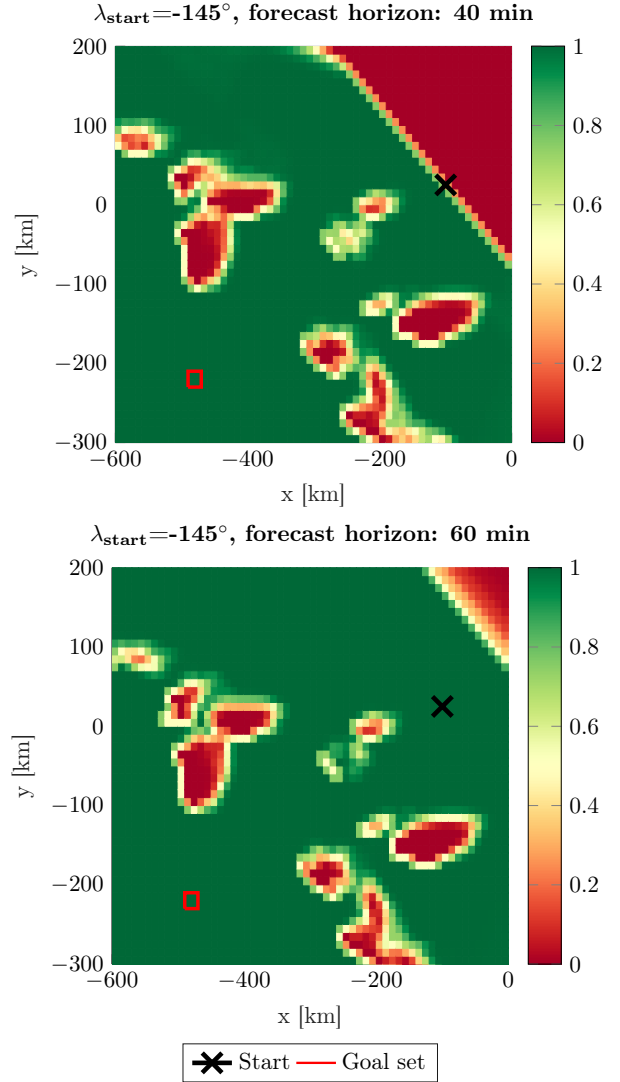


Figure 9: Maximum probability of reaching the desired waypoint while avoiding unsafe-fly regions, $V_0^*(\mathbf{s}_0)$ computed for flight 2, using two different forecast horizons.

fine simulation setting shows that both settings yield a safety-optimal solution. Choosing a finer resolution will potentially yield better performance in terms of flight time (and therefore fuel, CO_2 emissions, costs), as the increased accuracy in storm representation reduces the area of unsafe-fly regions. However, computational runtime increases significantly. The choice of resolution thus represents a trade-off between system performance in terms of flight time and computational runtime.

Flight 2; Setting 2. For flight 2 we keep the simulation settings 2, but change the initial conditions. Figure 11 shows the mean trajectory and 2σ confidence bounds out of 10'000 simulated realizations for two different time horizons: 40 and 60 minutes.

Due to the initial conditions on the aircraft state, in particular the long distance to the goal set (considering the limited range of 40 min flight time), the aircraft cannot take a right turn at the start to avoid the dangerous clusters ahead and to minimize

Table 4: Overview of simulation results.

	Flight 1		Flight 2	
Setting	1	2	2	2
Time horizon (min)	40	40	40	60
Flight time	1'824 s	1'776 s	2'280 s	2'340 s
Reach-avoid probability	1.00	1.00	0.56	1.00
Successful trajectories	100 %	100 %	88 %	95%

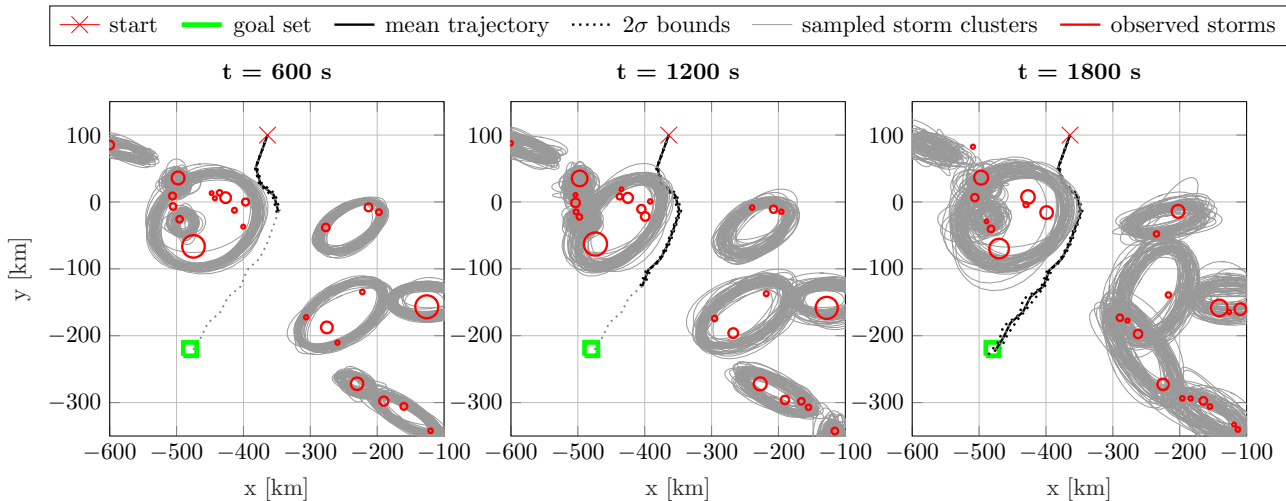


Figure 10: Flight 1, Setting 1: mean trajectory and 2σ trajectory bounds.

the risk of flying through a storm. Instead, the combined reach-avoid probability is maximized by a trajectory that trades storm avoidance for the ability to reach the goal set within the fixed horizon of 40 min. In reality, this would prevent the aircraft from choosing a route that avoids all storms, but fails to reach the target within the given time or fuel constraint, which could result in catastrophic failure. The resulting optimal reach-avoid probability is 0.56. Out of the 10'000 simulated trajectories, 8'773 reach the target. All of them avoid the observed storm cells in red. Some trajectories are forced to pass through forecast storm clusters. However, no storms are eventually observed in these areas. This explains the discrepancy between the value of the reach-avoid probability and the number of successful trajectories. Note that this discrepancy adds conservatism to the predicted safety of the generated trajectory and is not detrimental to safety.

We computed the maximum reach-avoid probability for flight 2 with an extended time horizon of 60 minutes. The aircraft now has the possibility to divert towards north of the predicted storm clusters. While the 40 minute trajectory reaches its goal at 2280 s on average, the 60 minute trajectory does not get as close to this time constraint, reaching the goal set after 2340 s on average. In contrast to the 40 minute time horizon, in the 60 minute horizon, 94% of the simulated trajectories reach the goal state while avoiding all observed storm cells. This confirms that the time horizon should be determined according to the available forecast data and underlines the importance of high-quality forecasts with extended forecast times. In prac-

tice, however, there may be fuel limitation or time of flight constraints for choosing the maximum time horizon.

5. Conclusions

We presented a novel approach to extract a probabilistic dynamic description of hazardous thunderstorm regions from state-of-the-art nowcast data. We integrated the stochastic thunderstorm model in a stochastic, optimal trajectory planning tool, which maximizes the probability of reaching a specified goal set while avoiding the hazardous thunderstorm regions. Simulations of different scenarios using historic nowcast files have proven the obstacle avoidance quality of the generated trajectories, as well as the accuracy of the computed safety levels. This information could be presented to both pilots and controllers to aid them in decision making processes. The computational performance is nevertheless not satisfactory for online implementation. The main reason is the curse of dimensionality inevitably resulting from the use of the dynamic programming approach in a 4D spatiotemporal space. Hence, the developed algorithm could be used in pre-tactical scenarios and as a benchmark tool to compare trajectories generated by other optimization approaches with the safety-optimal trajectories. To improve runtime, future work should explore alternative, more efficient numerical optimization methods such as nonlinear programming or chance-constrained optimization, and parallelized GPU computing. More efficient computational performance

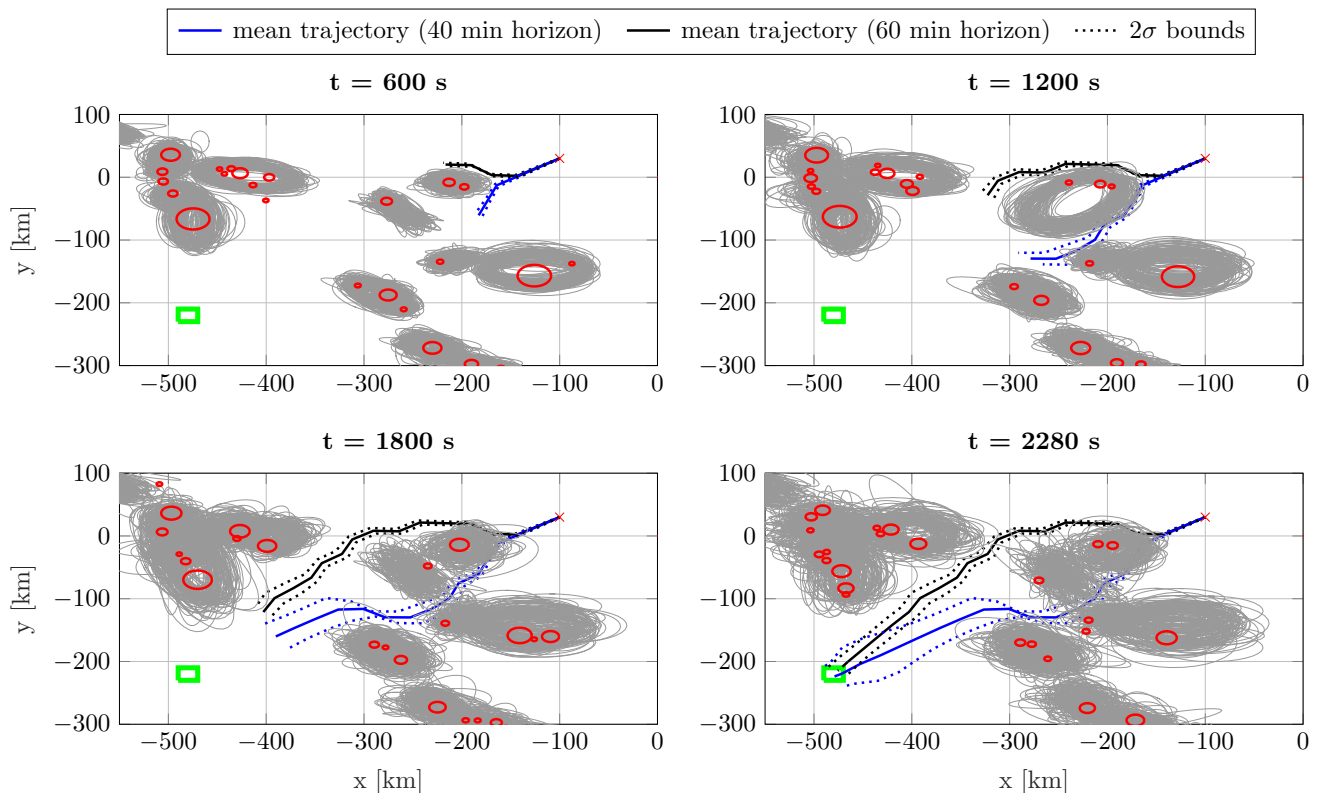


Figure 11: Flight 2, Setting 2: mean trajectory and 2σ trajectory bounds.

would also enable to explore control frameworks such as receding horizon control. This would enable replanning of the trajectory as new forecasts come in. Another potential field of future research is the incorporation of other adverse meteorological phenomena, e.g., wind-shear, hail, or clean air turbulence, into the presented framework, further maximizing safety.

Acknowledgments

We would like to thank the *Agencia Estatal de Meteorología* (AEMET) for kindly providing the nowcast data employed in this research. M. Kamgarpour thanks Swiss National Fund 200021_172782 for their partial support.

References

- B. Zhang, L.T., Roemer, M., 2014. Probabilistic weather forecasting analysis for unmanned aerial vehicle path planning. *Journal of Guidance, Control, and Dynamics* 37, 309–312.
- Browning, K., Collier, C., Larke, P., Menmuir, P., Monk, G., Owens, R.G., 1982. On the Forecasting of Frontal Rain Using a Weather Radar Network. *Mon. Wea. Rev.*, 534–552.
- European Commission, Eurocontrol, 2015. SESAR European ATM Master Plan, Edition 2015. URL: <https://ec.europa.eu/transport/modes/air/sesar/>, doi:10.2829/240873.
- Gonzalez-Arribas, D., Hentzen, D., Sanjurjo-Rivo, M., Kamgarpour, M., Soler, M., 2017. Optimal Aircraft Trajectory Planning in the Presence of Stochastic Convective Weather Cells, in: *AIAA Aviation 2017*, Denver, CO.
- Hentzen, D., 2017. Optimal Aircraft Trajectory Planning in Stochastic Environment. Semester Project. ETH Zurich, Zurich, Switzerland.
- Joint Planning and Development Office, 2012. Concept of Operations for the Next Generation Air Transportation System, Version 3.2. URL: <http://www.dtic.mil/dtic/tr/fulltext/u2/a535795.pdf>.
- Jung, Y., Xue, M., Zhang, G., Straka, J.M., 2008. Assimilation of simulated polarimetric radar data for a convective storm using the ensemble kalman filter. part ii: Impact of polarimetric data on storm analysis. *Monthly Weather Review* 136, 2246–2260.
- Kamgarpour, M., Dadok, V., Tomlin, C., 2010. Trajectory generation for aircraft subject to dynamic weather uncertainty. *49th IEEE Conference on Decision and Control*, 2063–2068.
- Kober, K., Tafferner, A., 2009. Tracking and nowcasting of convective cells using remote sensing data from radar and satellite. *Meteorologische Zeitschrift* 18, 75–84.
- Krozel, J., Mitchell, J., 2007. Capacity Estimation for Airspaces with Convective Weather Constraints. *AIAA Guidance, Navigation, and Control Conf.*, 1–15.
- Kuwata, Y., Schouwenaars, T., Richards, A., How, J., 2005. Robust Constrained Receding Horizon Control for Trajectory Planning. *AIAA Guidance, Navigation, and Control Conference and Exhibit*.
- Liu, W., Hwang, I., 2014. Probabilistic Aircraft Midair Conflict Resolution Using Stochastic Optimal Control. *IEEE Trans. Intell. Transp. Syst.* 15, 37–46.
- McNally, D., Sheth, K., Gong, C., Sterenchuk, M., Sahlman, S., Hinton, S., Lee, C., Shih, F.T., 2015. Dynamic weather routes: Two years of operational testing at american airlines. *Air Traffic Control Quarterly* 23, 55–81.
- Mecikalski, J.R., Williams, J.K., Jewett, C.P., Ahijevych, D., LeRoy, A., Walker, J.R., 2015. Probabilistic 0–1-h convective initiation nowcasts that combine geostationary satellite observations and numerical weather prediction model data. *Journal of Applied Meteorology and Climatology* 54, 1039–1059.
- Michalek, D., Balakrishnan, H., 2009. Identification of Robust Routes using

Convective Weather Forecasts. Eighth USA/Europe Air Traffic Management Research and Development Seminar , 1–10.

National Research Council, 2003. Weather Forecasting Accuracy for FAA Traffic Flow Management: A Workshop Report. Technical Report. Washington, DC.

Nilim, A., Ghaoui, L.E., Duong, V., 2002. Robust dynamic routing of aircraft under uncertainty, in: Proceedings. The 21st Digital Avionics Systems Conference, pp. 1A5–1–1A5–13 vol.1.

Osinski, R., Bouttier, F., 2018. Short-range probabilistic forecasting of convective risks for aviation based on a lagged-average-forecast ensemble approach. *Meteorological Applications* 25, 105–118.

Radhakrishna, B., Zawadzki, I., Fabry, F., 2012. Predictability of Precipitation from Continental Radar Images. Part V: Growth and Decay. *Journal of the Atmospheric Sciences* 69, 3336–3349.

Sauer, M., Hauf, T., 2014. Uncertainty Analysis of Thunderstorm Nowcasts for Utilization in Aircraft Routing, in: Fourth SESAR Innovation Days, Madrid, Spain.

Summers, S., Kamgarpour, M., Lygeros, J., Tomlin, C., 2011. A Stochastic Reach-avoid Problem with Random Obstacles, in: Proceedings of the 14th International Conference on Hybrid Systems: Computation and Control, ACM, New York, NY, USA. pp. 251–260.

Wilson, J.W., Crook, N.A., Mueller, C.K., Sun, J., Dixon, M., 1998. Nowcasting thunderstorms: A status report. *Bulletin of the American Meteorological Society* 79, 2079–2099.

Zhang, B., Tang, L., Roemer, M., 2017. Probabilistic planning and risk evaluation based on ensemble weather forecasting. *IEEE Transactions on Automation Science and Engineering* PP, 1–11.

Zinner, T., Mannstein, H., Tafferner, A., 2008. Cb-tram: Tracking and monitoring severe convection from onset over rapid development to mature phase using multi-channel meteosat-8 seviri data. *Meteorology and Atmospheric Physics* 101, 191–210.